

# Echo-E<sup>3</sup>Net: Efficient Endocardial Spatio-Temporal Network for Ejection Fraction Estimation

Moein Heidari<sup>✉</sup>, Member, IEEE, Afshin Bozorgpour<sup>✉</sup>, Member, IEEE, AmirHossein Zarif-Fakharnia<sup>✉</sup>, Wenjin Chen, Dorit

Merhof<sup>✉</sup>, Member, IEEE, D. J. Foran<sup>✉</sup>, Member, IEEE, Jasmine Grewal, and Ilker Hacihaliloglu<sup>✉</sup>, Member, IEEE

**Abstract**— Left ventricular ejection fraction (LVEF) is a key indicator of cardiac function and is routinely used to diagnose heart failure and guide treatment decisions. Although deep learning has advanced automated LVEF estimation, many existing approaches are computationally demanding and underutilize the joint structure of spatial and temporal information in echocardiography videos, limiting their suitability for real-time clinical deployment. We propose Echo-E<sup>3</sup>Net, an efficient endocardial spatio-temporal network specifically designed for LVEF estimation from echocardiography videos. Echo-E<sup>3</sup>Net comprises two complementary modules: (1) a dual-phase Endocardial Border Detector (E<sup>2</sup>CBD), which uses phase-specific cross-attention to predict ED/ES endocardial landmarks (EBs) and learn phase-aware landmark embeddings (LEs), and (2) an Endocardial Feature Aggregator (E<sup>2</sup>FA), which fuses these embeddings with global statistical descriptors (mean, maximum, variance) of deep feature maps to refine EF regression. A multi-component loss function, inspired by Simpson’s biplane method, jointly supervises EF, volumes, and landmark geometry, thereby aligning optimization with the clinical definition of LVEF and promoting robust spatio-temporal representation learning. Evaluated on the EchoNet-Dynamic dataset, Echo-E<sup>3</sup>Net achieves an RMSE of 5.20 and an R<sup>2</sup> score of 0.82, while using only 1.54M parameters and 8.05 GFLOPs. The model operates without external pre-training, heavy data augmentation, or test-time ensembling, making it highly suitable for real-time point-of-care ultrasound (POCUS) applications. Code is available at: <https://github.com/UltrAi-lab/Echo-E3Net>

**Index Terms**— Echocardiography, Attention mechanism, Ejection fraction, Point of care ultrasound (POCUS).

arXiv:2503.17543v2 [eess.IV] 6 Dec 2025

Manuscript submitted on < Month, Day, Year >. This work was supported by the Canadian Foundation for Innovation-John R. Evans Leaders Fund (CFI-JELF) program grant number 42816. Mitacs Accelerate program grant number AWD024298-IT33280. We also acknowledge the support of the Natural Sciences and Engineering Research Council of Canada (NSERC), [RGPIN-2023-03575]. Cette recherche a été financée par le Conseil de recherches en sciences naturelles et en génie du Canada (CRSNG), [RGPIN-2023-03575]. (Corresponding author: Ilker Hacihaliloglu.)

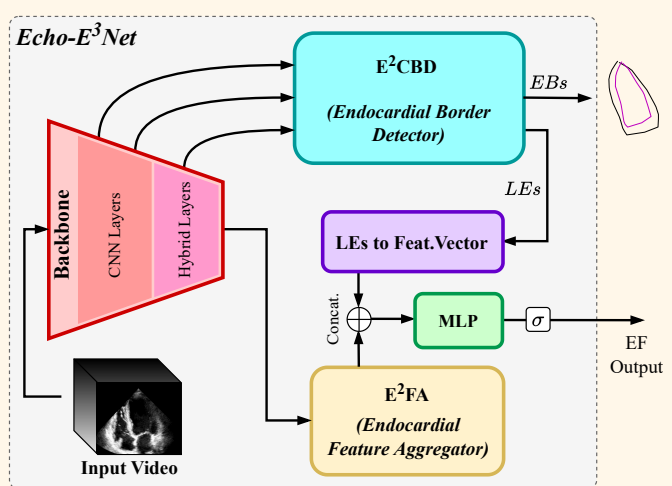
M. Heidari is with the School of Biomedical Engineering, The University of British Columbia, Vancouver, BC V6T 1Z4, Canada (e-mail: moein.heidari@ubc.ca).

A. Bozorgpour is with the Faculty of Informatics and Data Science, University of Regensburg, 93053 Regensburg, Germany (e-mail: afshin.bozorgpour@ur.de).

W. Chen is with the Biomedical Informatics Division, Rutgers Cancer Institute, Rutgers University, New Brunswick, NJ 08901 USA (e-mail: wenjin.chen@rutgers.edu).

A. Zarif-Fakharnia is with the Iran University of Science and Technology, Tehran, Iran (e-mail: a.zarif@alumni.iust.ac.ir).

D. Merhof is with the Chair of Image Analysis and Computer Vision, Faculty of Informatics and Data Science, University of Regensburg, 93053 Regensburg, Germany (e-mail: dorit.merhof@ur.de).



## I. INTRODUCTION

Left ventricular ejection fraction (LVEF) is one of the most critical indicators of cardiac function, used to assess heart failure and guide clinical decision-making [1]–[5]. LVEF is traditionally estimated using Simpson’s biplane method on two-dimensional (2D) echocardiographic images, which requires manual delineation of the left ventricle across mul-

D. J. Foran is with the Rutgers Cancer Institute and the Departments of Pathology, Laboratory Medicine and Radiology, Rutgers Robert Wood Johnson Medical School, Rutgers University, New Brunswick/Piscataway, NJ 08901 USA (e-mail: foran@cinj.rutgers.edu).

J. Grewal is with the Division of Cardiology, University of British Columbia, and St. Paul’s Hospital (Provincial Cardio-Obstetrics and Virani Provincial Adult Congenital Heart Programs), Vancouver, BC, Canada (e-mail: jagrewal@providencehealth.bc.ca).

I. Hacihaliloglu is with the Department of Radiology and the Department of Medicine, The University of British Columbia, Vancouver, BC V6T 1Z4, Canada (e-mail: ilker.hacihaliloglu@ubc.ca).

**Highlights**

- Echo-E<sup>3</sup>Net introduces a dual-phase endocardial border detector with Simpson-inspired geometric loss for efficient, anatomy-guided EF estimation.
- Echo-E<sup>3</sup>Net achieves strong performance on EF estimation on the EchoNet-Dynamic dataset using only 1.54M parameters and 8.05 GFLOPs.
- The method improves accuracy in clinically critical low-EF ranges and enables real-time POCUS deployment.

multiple cardiac phases [2]. However, this process is subject to high inter-observer variability and is time-intensive [6], [7]. To overcome these limitations, recent advancements in deep learning approaches have led to substantial improvements in the accuracy and robustness of EF estimation [1], [3], [5]. Several novel approaches have been proposed for estimating ejection fraction (EF) [4]. These include segmentation-based techniques [8], [9], direct video-level EF prediction methods [8], [10], [11], graph- and keypoint-guided strategies [1], [12], and models that incorporate attention mechanisms to enhance performance [13]. Despite their promise, these methods face key limitations that hinder real-world adoption—chief among them the challenge of maintaining high accuracy while minimizing computational overhead. This trade-off becomes particularly important for deployment on point-of-care ultrasound (POCUS) systems, where efficiency and reliability are critical [14].

POCUS, increasingly used for bedside cardiac assessment, offers substantial advantages in portability and rapid decision-making [15]. Yet reliable estimation of LVEF remains difficult due to operator-dependent variability, inconsistent acoustic windows, and fluctuating image quality [6]. These limitations highlight the need for computationally efficient and anatomically informed models that remain robust under real-world imaging conditions [16].

To address this challenge, the present work proposes an efficient architecture that incorporates explicit cardiac anatomy into the prediction process rather than treating EF estimation as a purely data-driven regression task. The framework uses a dual-phase Endocardial Border Detector (E<sup>2</sup>CBD), where end-diastolic and end-systolic queries attend to compressed multi-scale spatio-temporal tokens to localize ventricular boundaries. This yields both ED/ES landmark coordinates and phase-aware landmark embeddings, providing a compact descriptor of endocardial geometry and motion. Combined with a lightweight encoder, this formulation enables physiologically consistent and computationally efficient prediction.

**Contributions.** This study introduces Echo-E<sup>3</sup>Net, a compact framework that integrates explicit anatomical cues with global spatio-temporal features for robust LVEF estimation. The E<sup>2</sup>CBD module models ED/ES boundary structure, while the Endocardial Feature Aggregator (E<sup>2</sup>FA) fuses landmark embeddings with global statistical descriptors from deep feature maps. Model optimization is guided by a loss inspired by Simpson's biplane method, enforcing geometric coherence across phases. Despite using only 1.54M parameters and no external pre-training or heavy augmentation, Echo-E<sup>3</sup>Net achieves state-of-the-art performance with markedly

reduced computational cost, supporting real-time deployment in point-of-care ultrasound environments.

**II. RELATED WORKS**

Automated LVEF estimation from echocardiographic images has long been studied, with traditional methods relying on rule-based techniques and manual left ventricle segmentation, leading to notable inter-observer variability [6]. Owing to the surge of deep learning techniques, recent advancements in convolutional neural networks (CNNs), graph neural networks (GNNs), and transformer-based architectures have significantly enhanced the accuracy and efficiency of LVEF prediction [2]. In this regard, EchoNet-Dynamic leveraged CNNs to extract spatial features from echocardiographic video sequences and achieved SOTA accuracy in LVEF estimation [8]. Graph-based approaches, such as EchoGNN [1] and EchoGraphs [12], have demonstrated promising results by leveraging key point-based structural representations of the left ventricle. These methods improve interpretability by providing explicit shape constraints while reducing reliance on dense image-based CNN architectures [14], [17]. However, a notable drawback of these approaches is that they assign smaller weights to end-diastolic (ED) and end-systolic (ES) frames, which are clinically crucial for estimating ejection fraction, thereby diverging from standard clinical practices. To address data imbalance in LVEF regression tasks, EchoMEN [5] was proposed as a multi-expert network that dynamically weights different prediction models to optimize performance across a diverse dataset, but its reliance on multiple expert models increases computational overhead. EchoNarrator [4] employs a GCN framework to not only predict LVEF but also generate human-interpretable text explanations of the results [14]. Recently, Yang et al. [18] propose a reconstruction-based framework that leverages prior cardiac knowledge to capture local structural and motion anomalies in echocardiogram videos, while CoReEcho [7] estimates from 2D+time echocardiograms by focusing on continuous representation learning.

In contrast to prior methods, our approach is optimised to reduce computational burden while maintaining robust LVEF estimation accuracy, thereby enabling efficient and practical deployment in POCUS applications. Moreover, our work uniquely integrates anatomical guidance by explicitly modelling endocardial boundaries, as opposed to direct feature extraction from echocardiographic sequences. Lastly, we introduce a multi-component loss function tailored to align with the clinical definition of ejection fraction, ensuring a more robust and clinically meaningful estimation process.

### III. METHODOLOGY

#### A. Problem Formulation

Given an echocardiography dataset  $\mathcal{D} := \{(V^n, y^n)\}_{n=1}^N$ , each video  $V^n \in \mathbb{R}^{C \times F^n \times H \times W}$  consists of  $F^n \in \mathbb{Z}^+$  frames with spatial resolution  $H \times W$  and an associated left ventricular ejection fraction (EF) value  $y^n \in (0, 100)$ . For each study, we additionally have end-diastolic volume (EDV), end-systolic volume (ESV), and dual-phase (ED/ES) endocardial landmark annotations. The goal is to learn a model that, given an input echocardiographic video  $V^n$ , predicts the EF  $\hat{y}^n$  (and optionally EDV/ESV), while remaining consistent with the underlying cardiac geometry.

We propose Echo-E<sup>3</sup>Net, a 3D network that explicitly couples dual-phase endocardial border modeling with global spatio-temporal feature aggregation. As illustrated in Figure 2, the architecture comprises three main components:

- 1) a backbone encoder that extracts multi-scale 3D features,
- 2) a dual-phase Endocardial Border Detector (**E<sup>2</sup>CBD**) that predicts ED/ES landmarks and associated phase-aware landmark embeddings, and
- 3) an Endocardial Feature Aggregator (**E<sup>2</sup>FA**) that fuses these geometric descriptors with global statistics to regress EF and, when available, EDV/ESV.

E<sup>2</sup>CBD is trained with anatomically motivated geometric constraints derived from Simpson’s biplane method, while E<sup>2</sup>FA ensures that both local shape and global contractility cues contribute to the final prediction.

#### B. Backbone Network

We adopt the encoder of LHUNet [19] as our backbone for volumetric feature extraction. The encoder processes the input video  $V \in \mathbb{R}^{C \times F \times H \times W}$  and outputs a deepest feature map  $x \in \mathbb{R}^{B \times D_b \times T \times H_b \times W_b}$  together with a hierarchy of skip features  $\{s_i\}_{i=1}^L$ , where  $s_i \in \mathbb{R}^{B \times C_i \times T \times H_i \times W_i}$ . As illustrated in Figure 1, the encoder is organized into three stages. A point-wise convolution (PW-Conv) block first adapts the input channels. Subsequent purely convolutional blocks extract fine-grained local features while progressively downsampling the spatial dimensions. The final stage employs hybrid blocks that integrate large-kernel convolutions with channel-wise attention to capture long-range dependencies. Unlike the original LHUNet, which uses deformable convolutions for segmentation, we rely on static large kernels to maintain a wide receptive field at reduced computational cost. This design yields rich multi-scale 3D representations that serve as inputs to our E<sup>2</sup>CBD and E<sup>2</sup>FA modules.

#### C. Dual-Phase Endocardial Border Detector (**E<sup>2</sup>CBD**)

Clinical EF estimation relies on endocardial boundaries at end-diastole (ED) and end-systole (ES). The E<sup>2</sup>CBD module is designed to mirror this workflow by jointly predicting ED/ES landmarks and phase-aware landmark embeddings. Rather than relying on image-agnostic templates, landmarks are obtained through phase-specific cross-attention over multi-scale 3D tokens, ensuring that the predicted borders remain anatomically meaningful.

**1) Multi-scale Spatio-Temporal Tokenization:** E<sup>2</sup>CBD operates on the skip features  $\{s_i\}_{i=1}^{L-1}$  from the encoder (we exclude the coarsest scale to limit memory and focus on spatially informative resolutions). For each level  $i$ , we first project the channels to a common hidden dimension  $h$  using a point-wise convolution:

$$\tilde{s}_i = \phi_i(s_i) \in \mathbb{R}^{B \times h \times T \times H_i \times W_i}, \quad (1)$$

where  $\phi_i$  denotes the projection. To preserve spatio-temporal structure, we augment  $\tilde{s}_i$  with learnable positional and level embeddings. We construct a normalized 3D coordinate grid  $(t, y, x) \in [-1, 1]^3$  and map it through a linear layer  $P_{\text{pos}} : \mathbb{R}^3 \rightarrow \mathbb{R}^h$  to obtain position encodings for each spatio-temporal location. Additionally, we use a learned level embedding  $p_{\text{lvl},i} \in \mathbb{R}^h$  to distinguish different pyramid scales. The resulting features are

$$\hat{s}_i = \tilde{s}_i + P_{\text{pos}}(t, y, x) + p_{\text{lvl},i}. \quad (2)$$

This design makes the subsequent attention layers aware of both absolute space-time coordinates and relative scale.

We then flatten  $\hat{s}_i$  over the temporal and spatial dimensions into a sequence of tokens of length  $N_i = TH_iW_i$ :

$$f_i \in \mathbb{R}^{B \times N_i \times h}. \quad (3)$$

The tokens from all levels are concatenated to form a multi-scale token set

$$f = [f_1; \dots; f_{L-1}] \in \mathbb{R}^{B \times N_s \times h}, \quad (4)$$

where  $N_s = \sum_i N_i$ . Directly attending over all  $N_s$  tokens is memory-intensive for 3D data. To control memory usage without losing global context, we introduce a token budget  $N_{\text{max}}$ ; if  $N_s > N_{\text{max}}$ , we uniformly subsample tokens along the sequence dimension to obtain a compressed token set  $f' \in \mathbb{R}^{B \times N_{\text{eff}} \times h}$ , where  $N_{\text{eff}} = \min(N_s, N_{\text{max}})$ . A lightweight fusion layer (Linear-LayerNorm-GELU) refines these tokens:

$$z = \text{Fusion}(f') \in \mathbb{R}^{B \times N_{\text{eff}} \times h}. \quad (5)$$

This multi-scale tokenization and compression provides a compact yet expressive representation over which E<sup>2</sup>CBD can operate efficiently.

#### 2) Phase-Specific Cross-Attention and Landmark Decoding:

To explicitly model the two key cardiac phases, we introduce two banks of landmark queries,  $Q^{\text{ED}}, Q^{\text{ES}} \in \mathbb{R}^{L \times h}$ , each containing  $L$  learnable query vectors, one per landmark. For each phase, the corresponding queries attend to the multi-scale token set via multi-head cross-attention:

$$E^{\text{phase}} = \text{MHA}(Q^{\text{phase}}, z, z) \in \mathbb{R}^{L \times h}, \quad \text{phase} \in \{\text{ED}, \text{ES}\}, \quad (6)$$

where  $z$  serves as both keys and values, and we use  $h = 32$  with 4 attention heads. In practice, we apply this operation in batch-first form, yielding  $E^{\text{ED}}, E^{\text{ES}} \in \mathbb{R}^{B \times L \times h}$ . These phase-specific landmark embeddings (LEs) summarize where and how the network attends to the video when predicting each landmark, capturing both spatial location and local appearance/motion cues.

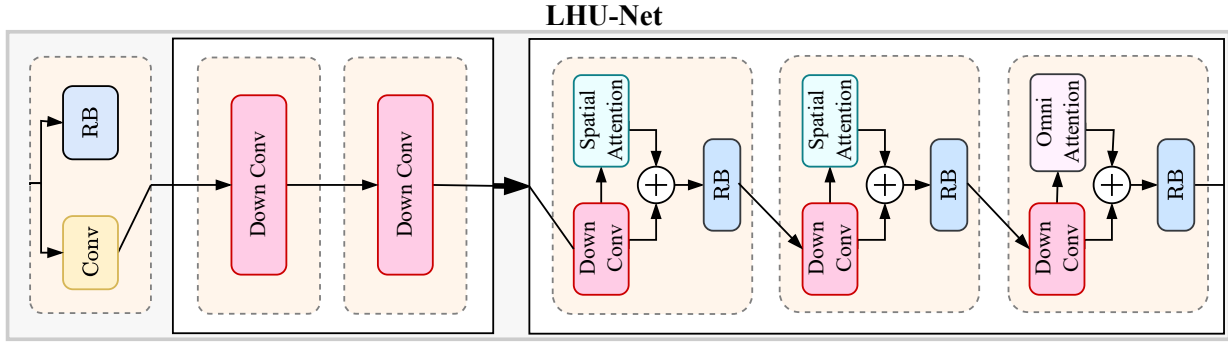


**Fig. 1:** Overview of the LHUNet encoder architecture [19]. The encoder produces multi-scale spatio-temporal features; we use the deepest feature map for global aggregation and the skip features as inputs to our  $E^2$ CBD module.

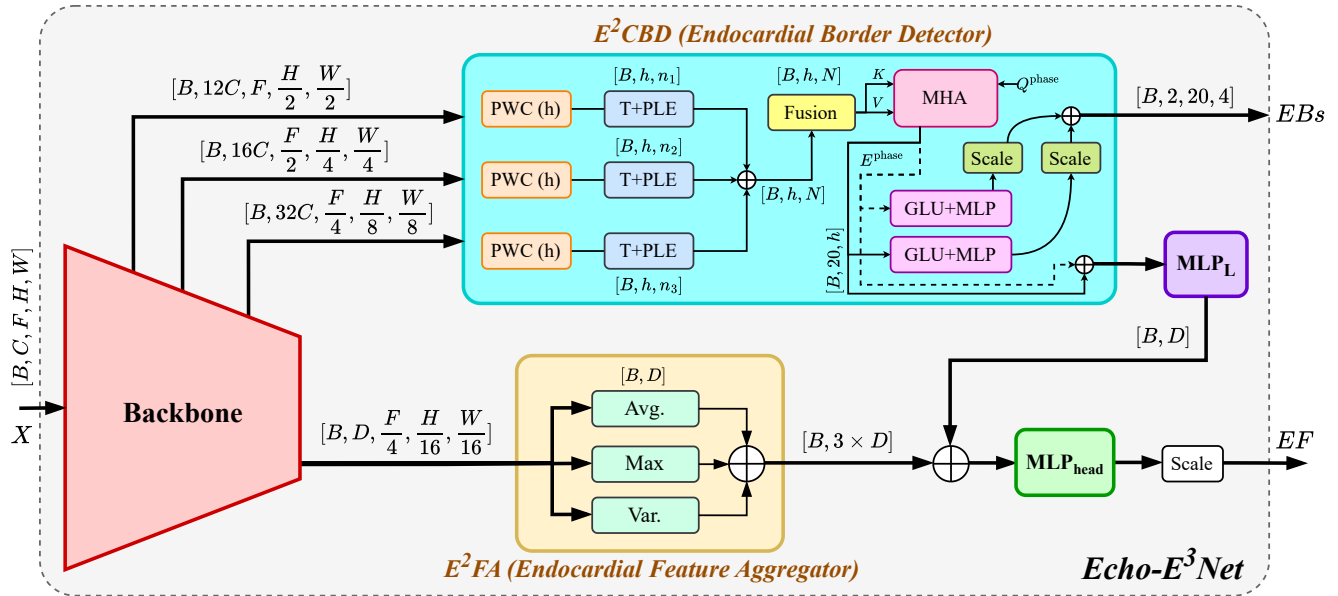


**Fig. 2:** Overall architecture of Echo-E<sup>3</sup>Net. The input echocardiographic video is processed by the LHUNet encoder to produce multi-scale spatio-temporal features. The  $E^2$ CBD module applies phase-specific cross-attention from ED/ES landmark queries to the multi-scale token set, yielding explicit dual-phase landmark coordinates and corresponding landmark embeddings. The  $E^2$ FA module aggregates global statistics (average, maximum, variance) from the deepest feature map and fuses them with the landmark descriptor to regress EF and, when available, EDV/ESV.

Each phase-specific embedding is then decoded into 2D coordinates using a small MLP followed by a gated linear unit (GLU) refiner:

$$c^{\text{phase}} = \text{GLU}(\text{MLP}(E^{\text{phase}})) \in \mathbb{R}^{B \times L \times 4}, \quad (7)$$

where each landmark is parameterized as  $(x_1, y_1, x_2, y_2)$  so that contour segments can be represented by pairs of points. We apply a  $\tanh$  nonlinearity and scale the outputs to match the normalized image grid:

$$\ell^{\text{phase}} = \frac{\text{coord\_scale}}{2} (\tanh(c^{\text{phase}}) + 1), \quad (8)$$

with  $\text{coord\_scale} = 112$  in our experiments. This constrains the coordinates to  $[0, \text{coord\_scale}]$  and facilitates stable training by preventing unbounded predictions.

Finally, we stack the ED and ES landmarks to obtain

$$\mathcal{L}_{\text{CBD}} = \{\ell^{\text{ED}}, \ell^{\text{ES}}\} \in \mathbb{R}^{B \times 2 \times L \times 4}, \quad (9)$$

and similarly stack the corresponding embeddings  $E^{\text{ED}}, E^{\text{ES}}$  to form

$$\mathcal{E}_{\text{CBD}} \in \mathbb{R}^{B \times 2 \times L \times h}. \quad (10)$$

The coordinates  $\mathcal{L}_{\text{CBD}}$  are used for geometric supervision and qualitative visualization, while the embeddings  $\mathcal{E}_{\text{CBD}}$  serve as rich, phase-aware descriptors that are fed into the EF head. This decouples the EF regressor from noise in the raw coordinates while still grounding it in anatomically meaningful landmark predictions.

#### D. Endocardial Feature Aggregator ( $E^2$ FA)

Although  $E^2$ CBD provides explicit ED/ES border information, accurate EF estimation also requires robust global representations of LV contractility over the entire cardiac cycle. The  $E^2$ FA module aggregates complementary descriptors from the deepest backbone feature and the  $E^2$ CBD outputs.

Let  $x \in \mathbb{R}^{B \times D_b \times T \times H_b \times W_b}$  denote the deepest feature map from the encoder. We compute three global statistics across the spatio-temporal dimensions:

$$x_{\text{avg}} = \text{AvgPool}(x), \quad (11)$$

$$x_{\text{max}} = \text{MaxPool}(x), \quad (12)$$

$$x_{\text{var}} = \text{Var}(x), \quad (13)$$

where all operations produce tensors of shape  $\mathbb{R}^{B \times D_b \times 1 \times 1 \times 1}$ . These statistics summarize the mean intensity, peak response, and temporal-spatial variability of the LV across the sequence and have been empirically found to stabilize EF regression. In parallel, we compress the dual-phase landmark information ( $\mathcal{E}_{\text{CBD}}$ ) into a compact descriptor ( $v_{\text{Ind}}$ ):

$$v_{\text{Ind}} = \text{vec}(\mathcal{E}_{\text{CBD}}) \in \mathbb{R}^{B \times 2 \times L \times h}, \quad (14)$$

aligned with the backbone feature space. A small MLP projects  $v_{\text{Ind}}$  to the backbone channel dimension:

$$x_{\text{Ind}} = \text{MLP}_L(v_{\text{Ind}}) \in \mathbb{R}^{B \times D_b}, \quad (15)$$

which is then reshaped to  $\mathbb{R}^{B \times D_b \times 1 \times 1 \times 1}$ . In our main configuration, we use the embedding-based variant, which allows the EF head to exploit rich, phase-aware features that remain grounded in explicit landmark supervision. The coordinate-based variant is used as an ablation to quantify the benefit of attending to embeddings rather than directly to raw coordinates.

The final representation is obtained by concatenating the global statistics with the landmark descriptor:

$$F_{\text{final}} = [x_{\text{avg}}, x_{\text{max}}, x_{\text{var}}, x_{\text{Ind}}], \quad (16)$$

followed by flattening and passing through an MLP head. When full supervision is available, the head outputs three quantities:

$$[\widehat{\text{ESV}}, \widehat{\text{EDV}}, z_{\text{EF}}] = \text{MLP}_{\text{head}}(F_{\text{final}}), \quad (17)$$

and EF is computed as

$$\widehat{\text{EF}} = \frac{1}{2} (\tanh(z_{\text{EF}}) + 1) \times 100, \quad (18)$$

which constrains EF to (0, 100). When only EF labels are available, the head reduces to a single output with the same scaling. This design allows Echo-E<sup>3</sup>Net to seamlessly support datasets with and without volumetric labels, while always leveraging the geometric constraints imposed by E<sup>2</sup>CBD.

### E. Loss Functions

To align optimization with the clinical workflow of Simpson's biplane method, we design a composite loss that supervises both the global EF value and the geometry of the predicted LV endocardial chords. As illustrated in Figs. 3–4, clinicians obtain EF by tracing the LV in apical views, measuring diameters along the long axis, and integrating a stack of disks to estimate EDV and ESV. We mimic this procedure in a fully differentiable way at training time by turning the E<sup>2</sup>CBD landmarks into approximate Simpson disks and penalizing discrepancies between the predicted and reference geometry.

**1) Direct EF Regression:** The primary target of the network is the ejection fraction. Let  $\widehat{\text{EF}}_n$  and  $\text{EF}_n^{\text{gt}}$  denote the predicted and ground-truth EF for the  $n$ -th sequence in a batch of size  $N$ . We use a mean-squared error (MSE) loss:

$$\mathcal{L}_{\text{EF}} = \frac{1}{N} \sum_{n=1}^N (\widehat{\text{EF}}_n - \text{EF}_n^{\text{gt}})^2. \quad (19)$$

This term directly supervises the EF head and remains the dominant driver of optimization.

**2) Simpson-Inspired Geometric Supervision:** In addition to  $\mathcal{L}_{\text{EF}}$ , we impose geometric constraints on the LV chords produced by E<sup>2</sup>CBD. For each sample  $n$ , we denote the predicted ED and ES chords by  $\mathcal{L}_n^{\text{pd}} = \{\ell_{n,\phi,i}^{\text{pd}}\}$  and the corresponding reference chords by  $\mathcal{L}_n^{\text{gt}} = \{\ell_{n,\phi,i}^{\text{gt}}\}$ , where  $\phi \in \{\text{ED}, \text{ES}\}$  indexes the phase and  $i = 1, \dots, L$  indexes chords along the LV long axis from apex to mitral annulus (cf. Fig. 3). Each chord  $\ell_{n,\phi,i} = (x_{n,\phi,i}^{(1)}, y_{n,\phi,i}^{(1)}, x_{n,\phi,i}^{(2)}, y_{n,\phi,i}^{(2)})$  represents a pair of opposing endocardial points.

**a) Differentiable Simpson surrogate.:** Following the clinical workflow in Fig. 3 and the schematic in Fig. 4, we convert these chords into a stack of disks. For phase  $\phi \in \{\text{ED}, \text{ES}\}$  and level  $i \geq 2$ , we define the diameter of the disk as the Euclidean distance between the chord endpoints:

$$B_{n,\phi,i} = \|\mathbf{p}_{n,\phi,i}^{(1)} - \mathbf{p}_{n,\phi,i}^{(2)}\|_2, \quad (20)$$

where  $\mathbf{p}_{n,\phi,i}^{(1)} = (x_{n,\phi,i}^{(1)}, y_{n,\phi,i}^{(1)})$  and  $\mathbf{p}_{n,\phi,i}^{(2)} = (x_{n,\phi,i}^{(2)}, y_{n,\phi,i}^{(2)})$ . We approximate the height of the disk as the perpendicular distance between the center of the previous chord and the line defined by the current chord:

$$\mathbf{c}_{n,\phi,i-1} = \frac{1}{2} (\mathbf{p}_{n,\phi,i-1}^{(1)} + \mathbf{p}_{n,\phi,i-1}^{(2)}), \quad (21)$$

$$H_{n,\phi,i} = \text{dist}(\mathbf{c}_{n,\phi,i-1}, \text{line}(\mathbf{p}_{n,\phi,i}^{(1)}, \mathbf{p}_{n,\phi,i}^{(2)})). \quad (22)$$

The contribution of level  $i$  to the LV cavity volume at phase  $\phi$  is then

$$v_{n,\phi,i} = \pi \left( \frac{B_{n,\phi,i}}{2} \right)^2 H_{n,\phi,i}, \quad (23)$$

so that the total volume for phase  $\phi$  is

$$V_{n,\phi} = \sum_{i=2}^L v_{n,\phi,i}. \quad (24)$$

For the chord sets derived from ED and ES frames, this construction yields Simpson-like surrogates of EDV and ESV, from which a purely geometric EF surrogate can be computed as  $\widetilde{\text{EF}}_n = (V_{n,\text{ED}} - V_{n,\text{ES}})/V_{n,\text{ED}} \times 100$ . Our implementation applies this procedure to both predicted and ground-truth chords and returns the corresponding diameters  $\mathbf{B}_{n,\phi} = \{B_{n,\phi,i}\}$ , disk volumes  $\mathbf{v}_{n,\phi} = \{v_{n,\phi,i}\}$ , and per-phase long-axis measures  $\mathbf{H}_{n,\phi}$ .

**b) Pointwise landmark loss.:** We first enforce accurate localization of the chords themselves via an MSE loss on the coordinates:

$$\mathcal{L}_{\text{pts}} = \frac{1}{N} \sum_{n=1}^N \|\mathcal{L}_n^{\text{pd}} - \mathcal{L}_n^{\text{gt}}\|_2^2. \quad (25)$$

This term anchors the predicted chords to the reference ED/ES borders.

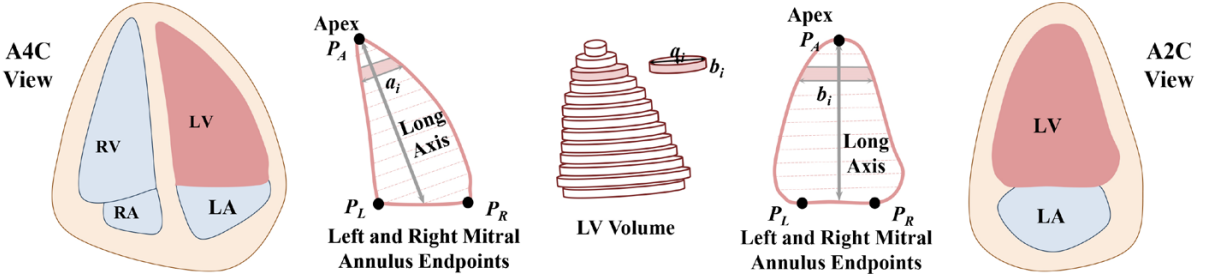


**Fig. 3:** Left ventricular measurements using the biplane Simpson's method (Figure adapted from [20]). The clinical workflow relies on accurate localization of key landmarks (apex and mitral annulus endpoints) to define the LV long axis, followed by diameter measurements at multiple levels and volumetric integration using stacked elliptical disks. Our geometric losses are inspired by these principles.

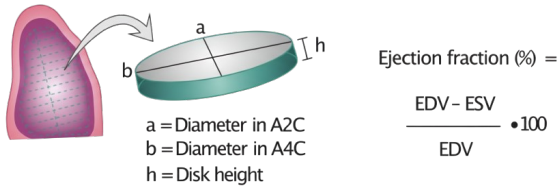


**Fig. 4:** Illustration of Simpson's biplane method (Figure adapted from [21]). LV volume is computed by stacking elliptical disks with diameters  $a$  and  $b$  and height  $h$ . Translating this into differentiable constraints allows us to regularize landmark predictions without explicit volumetric integration at inference time.

*c) Diameter and tapering losses.:* Simpson's method relies on physiologically plausible LV widths along the long axis. We therefore penalize mismatches between the diameters of the predicted and reference disks:

$$\mathcal{L}_B = \frac{1}{N} \sum_{n=1}^N \sum_{\phi \in \{\text{ED,ES}\}} \sum_{i=2}^L (B_{n,\phi,i}^{\text{pd}} - B_{n,\phi,i}^{\text{gt}})^2. \quad (26)$$

To encourage realistic tapering of the cavity, we additionally match the change in diameter between neighboring disks. Let  $\Delta B_{n,\phi,i} = B_{n,\phi,i+1} - B_{n,\phi,i}$  denote the discrete derivative along the long axis. We define

$$\mathcal{L}_{\Delta B} = \frac{1}{N} \sum_{n=1}^N \sum_{\phi \in \{\text{ED,ES}\}} \sum_{i=2}^{L-1} (\Delta B_{n,\phi,i}^{\text{pd}} - \Delta B_{n,\phi,i}^{\text{gt}})^2, \quad (27)$$

which penalizes unrealistic abrupt changes in LV width and stabilizes the Simpson volumes.

*d) Long-axis consistency loss.:* Finally, we regularize the effective long-axis measure of the cavity at ED and ES. Let  $\mathbf{H}_{n,\phi}^{\text{pd}}$  and  $\mathbf{H}_{n,\phi}^{\text{gt}}$  denote the sets of disk heights constructed above for phase  $\phi$ . We impose

$$\mathcal{L}_H = \frac{1}{N} \sum_{n=1}^N \sum_{\phi \in \{\text{ED,ES}\}} \|\mathbf{H}_{n,\phi}^{\text{pd}} - \mathbf{H}_{n,\phi}^{\text{gt}}\|_2^2, \quad (28)$$

which ensures that the predicted chords reproduce the overall LV length and spacing pattern used in Simpson's integration.

*e) Geometric loss and final objective.:* The Simpson-inspired geometric regularizer is then

$$\mathcal{L}_{\text{geo}} = \mathcal{L}_{\text{pts}} + \mathcal{L}_B + \mathcal{L}_{\Delta B} + \mathcal{L}_H. \quad (29)$$

The final EF-specific training objective combines direct EF regression with this geometric regularizer:

$$\mathcal{L}_{\text{total}} = \mathcal{L}_{\text{EF}} + \lambda_{\text{geo}} \mathcal{L}_{\text{geo}}, \quad (30)$$

where ( $\lambda_{\text{geo}} = 0.05$ ) is a small scalar chosen to keep the geometric terms within the same order of magnitude as the EF loss while preventing them from dominating the optimization. Importantly, all Simpson-related quantities (diameters, heights, disk volumes, and the geometric EF surrogate) are computed only during training from the E<sup>2</sup>CBD chords; at inference time the model outputs EF directly without performing any explicit volumetric integration.

#### IV. EXPERIMENTS

**Dataset and Evaluation Metrics.** We utilise the EchoNet-Dynamic dataset [8], comprising 10,030 A4C echocardiography videos collected from Stanford University Hospital between 2016 and 2018. Each video consists of  $112 \times 112$  grayscale image sequences, annotated with 40 left ventricular (LV) contour points (as outlined in the output of E<sup>2</sup>CBD module), along with one basal and apex point at both end-diastolic (ED) and end-systolic (ES) frames, and the corresponding ejection fraction (EF). We adopt the standard training, validation, and test splits provided by EchoNet for benchmarking. We evaluate model performance using mean absolute error (MAE), root mean squared error (RMSE), and R-squared ( $R^2$ ) as primary metrics. Additionally, we compare floating point operations (FLOPs) and model parameter counts in million (Params (M)) across different architectures to provide a comprehensive assessment of computational efficiency.

**Experimental Setup.** Deep learning models typically require a fixed frame count per video scan, while EchoNet-Dynamic videos contain varying cardiac cycle lengths (20–30 frames). To handle this variability, we employ adaptive frame sampling, where during training, an initial frame index  $k$  is uniformly sampled from  $[1, F_{\text{max}}^n - F_{\text{sel}}]$ , where  $F_{\text{max}}^n$  represents the total number of frames in echocardiography video  $n$  and use

**TABLE I:** Comparison of different EF estimation models on the EchoNet-Dynamic dataset. The abbreviations **R.** and **M.** correspond to the *Random* and *Mirroring* sampling strategies introduced in [22]. The EchoNet-Dynamic model is evaluated in two configurations: **(1)** estimating left ventricular ejection fraction (LVEF) at the clip level using 32 frames, and **(2)** incorporating segmentation alongside clip-level predictions to generate beat-to-beat LVEF estimates across the full video sequence. The parameter count is expressed in millions. **Blue**, and **Red** colors show best and second best.

Model	Frames	FLOPs	Params	MAE ↓	RMSE ↓	$R^2 \uparrow$
UVT R. [22]	128	130.00G	-	6.77	8.70	0.48
UVT M. [22]	128	130.00G	-	5.95	8.38	0.52
R3D [8]	32	92.273G	-	4.22	5.62	0.79
MC3 [8]	32	97.656G	-	4.45	5.68	0.76
EchoGNN [1]	64	-	<b>1.7</b>	4.45	-	0.77
EchoNet-Dynamic [8] (1)	32	91.974G	32	4.22	5.56	0.79
EchoNet-Dynamic [8] (2)	beat-to-beat	-	32	4.05	5.32	<b>0.81</b>
EchoGraphs [12] (2)		40.739G	27.6	4.01	5.36	<b>0.81</b>
EchoCoTr-B [11]	36	44.907G	21	3.98	5.34	<b>0.81</b>
EchoCoTr-S [11]	36	<b>19.611G</b>	-	3.95	<b>5.17</b>	<b>0.82</b>
CoReEcho [7]	36	58.92G	21	<b>3.90</b>	<b>5.13</b>	<b>0.82</b>
CardiacNet [18]	16	7949G	28	<b>3.83</b>	-	-
<b>Echo-E<sup>3</sup>Net (Ours)</b>	64	<b>8.05G</b>	<b>1.54</b>	3.93	5.20	<b>0.82</b>

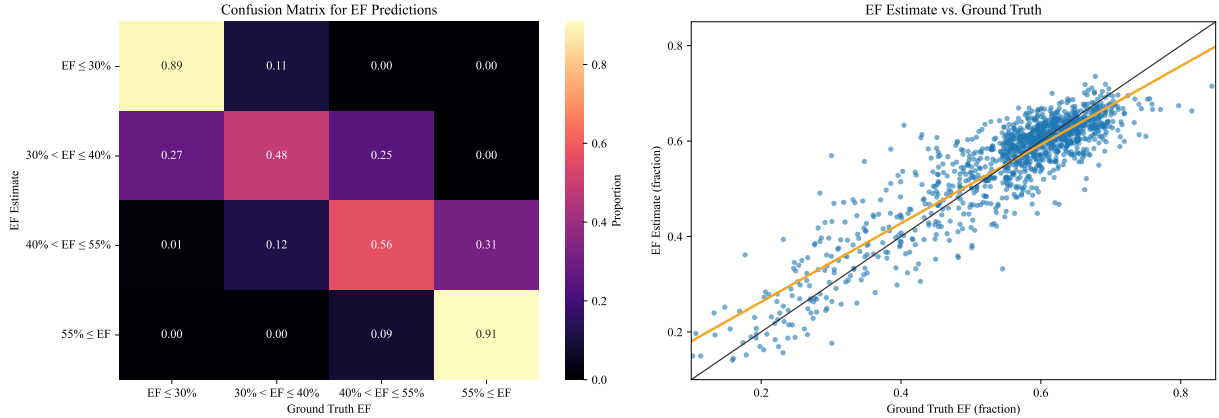


**Fig. 5:** (Left) The confusion matrix of our top-performing model. (Right) The scatter plot of our model’s EF predictions with the actual values.

$F_{\text{sel}}$  samples starting from  $k$  [1]. Following prior work [8], [11], we set  $F_{\text{sel}} = 64$  frames with a sampling frequency of 2. Unlike prior work [1], [11], for shorter videos where  $F_{\text{max}}^n < F_{\text{sel}}$ , we fill missing frames using the average of previous frames rather than zero-padding, as this approach better preserves temporal consistency. Our model was trained for 45 epochs on an NVIDIA RTX 4070 GPU, equipped with 12GB memory using a batch size of 16 which took 2 hours, much less than similar works (In our experiments, training EchoGraphs [12] required approximately one week.). We employ AdamW as optimizer, setting the learning rate and weight decay to 1e-4. A notable advantage of our approach over prior work is its ability to achieve high performance without relying on pretraining, data augmentation or ensemble models. In contrast, all existing methods incorporate either of them. For instance, [1] utilises ES and ED classification as a pre-training step, while [11] leverages pretrained models from the vision domain. EchoGraphs [12] performs extensive data augmentation techniques. Our method eliminates these dependencies, demonstrating effective learning without additional supervision.

## V. RESULTS

We evaluate Echo-E<sup>3</sup>Net against recent EF regression baselines as shown in table I. For a fair comparison, we utilize each method’s original configuration to maintain consistency with reported results. The quantitative evaluation, presented in table I, demonstrates that Echo-E<sup>3</sup>Net achieves either on-par or SOTA performance across multiple evaluation metrics, highlighting its effectiveness in EF estimation. These results are obtained while achieving substantially higher computational and memory efficiency, utilizing much fewer parameters and FLOPs compared to baselines. Specifically, while achieving competing results with CoReEcho [7] and CardiacNet [18], Echo-E<sup>3</sup>Net operates with just 8.05 GFLOPs, reducing compute by 86.3% vs. CoReEcho (58.92G) and 99.9% vs. CardiacNet (7949G). Moreover, it requires only 1.54M parameters, making it 92.7% and 94.5% more compact than CoReEcho and CardiacNet, respectively, indicating that Echo-E<sup>3</sup>Net demonstrates potential for deployment in POCUS environments, where computational resources are constrained. Figure 5 presents the confusion matrix of our best-performing model, highlighting EF categories associated with heart failure

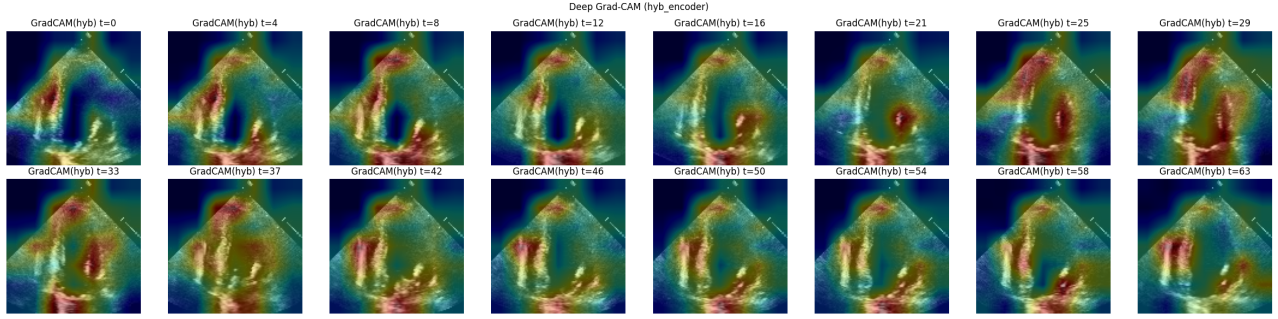


**Fig. 6:** Grad-CAM [23]. Echo-E<sup>3</sup>Net demonstrates reduced attention to background while enhancing focus on the LV, attributed to the effectiveness of the boundary detection module.

**TABLE II:** Ablation study assessing the contribution of the E<sup>2</sup>CBD and E<sup>2</sup>FA modules in Echo-E<sup>3</sup>Net.

Model Configuration	MAE ↓	RMSE ↓	R <sup>2</sup> ↑	Params (M)
W/o E <sup>2</sup> CBD	4.07	5.43	0.80	<b>1.42</b>
W/o E <sup>2</sup> FA	3.96	5.33	0.81	1.54
<b>Echo-E<sup>3</sup>Net (E<sup>2</sup>CBD + E<sup>2</sup>FA)</b>	<b>3.93</b>	<b>5.20</b>	<b>0.82</b>	1.54

risk. The scatter plot demonstrates the alignment between predicted and actual EF values. The training set of EchoNet-Dynamic exhibits an imbalanced distribution, with only 12.7% of samples having an EF ratio below 40%. However, from a clinical perspective, identifying these patients is crucial for timely intervention [1], [24], [25].

Notably, our model achieves clearly superior performance in the reduced-ejection-fraction range (EF < 40%), which is a clinically critical interval that typically prompts closer follow-up and therapy adjustment. Compared with EchoGNN [1], our confusion matrix shows higher on-diagonal proportions in both the EF ≤ 30% and 30% < EF ≤ 40% bins and fewer misclassifications into preserved-EF categories; likewise, the scatter plot exhibits tighter clustering around the identity line at low EF values. Together, these findings indicate that our method detects systolic dysfunction more reliably than the prior SOTA [1]. Moreover, table II presents the effect of ablating individual components of Echo-E<sup>3</sup>Net. Each removal leads to a degradation in performance, reflected by increased MAE and RMSE and decreased  $R^2$  while incorporating all components achieves the optimal results. Figure 6 visualizes Grad-CAM activations [23] of Echo-E<sup>3</sup>Net’s hybrid encoder block across different frames of a sample test video. The activation maps are tightly concentrated along the left-ventricular cavity and endocardial borders, with minimal response in the atria and surrounding background tissue. This focused pattern reflects the effect of the E<sup>2</sup>CBD module, which encourages the network to base its EF prediction on anatomically meaningful endocardial motion rather than spurious background cues.

Finally, we assess the real-time performance of our method by measuring wall-clock latency on a CPU-only workstation (Python 3.10, 64 frames at 112 × 112 resolution). After five warm-up passes, we time 50 forward passes with batch size 1. Echo-E<sup>3</sup>Net achieves a median latency of 45.5 ms per clip, corresponding to 22 clips/s. Given that echocardiographic cine loops are typically acquired at ≤ 15 fps, this throughput satis-

fies real-time constraints even on CPU hardware, underscoring the deployment readiness of our approach.

## VI. CONCLUSION

In this work, we introduced Echo-E<sup>3</sup>Net, an efficient endocardial spatio-temporal network for LVEF estimation from echocardiography videos. The model combines a lightweight hybrid backbone with spatial and channel attention to capture fine-grained ventricular dynamics, and an endocardial border detector that predicts dual-phase landmarks and associated embeddings aligned with the clinical workflow of Simpson’s method. A Simpson-inspired geometric loss jointly supervises EF, volumes, and landmark geometry, encouraging physiologically plausible predictions and improving performance in clinically critical low-EF ranges. Echo-E<sup>3</sup>Net achieves state-of-the-art accuracy on the EchoNet-Dynamic benchmark while using only 1.54M parameters and 8.05 GFLOPs, and attains real-time throughput on CPU, indicating strong potential for deployment in resource-constrained POCUS environments. Future work will focus on validating the framework across multi-view and multi-center datasets, extending it to additional quantitative indices (e.g., EDV/ESV and strain), and evaluating its impact in prospective, real-world POCUS workflows.

## REFERENCES

[1] M. Mokhtari, T. Tsang, P. Abolmaesumi, and R. Liao, "Echognn: explainable ejection fraction estimation with graph neural networks," in *International Conference on Medical Image Computing and Computer-Assisted Intervention*. Springer, 2022, pp. 360–369.

[2] M. Muldoon and N. Khan, "Lightweight and interpretable left ventricular ejection fraction estimation using mobile u-net," *IEEE ISBI*, 2023.

[3] R. Muhtaseb and M. Yaqub, "Echocotr: Estimation of the left ventricular ejection fraction from spatiotemporal echocardiography," *arXiv*, 2022.

[4] S. Thomas, Q. Cao, A. Novikova, D. Kulikova, and G. Ben-Yosef, "Echonarrator: Generating natural text explanations for ejection fraction predictions," *arXiv*, 2024.

[5] S. Lai, M. Zhao, Z. Zhao, S. Chang, X. Yuan, H. Liu, Q. Zhang, and G. Meng, "Echomen: Combating data imbalance in ejection fraction regression via multi-expert network," in *International Conference on Medical Image Computing and Computer-Assisted Intervention*. Springer, 2024, pp. 624–633.

[6] A. e. a. Ostvik, "Real-time automatic ejection fraction and foreshortening detection using deep learning," *IEEE Transactions on Ultrasonics, Ferroelectrics, and Frequency Control*, 2020.

[7] F. A. Maani, N. Saeed, A. Matsun, and M. Yaqub, "Coreecho: Continuous representation learning for 2d+ time echocardiography analysis," in *International Conference on Medical Image Computing and Computer-Assisted Intervention*. Springer, 2024, pp. 591–601.

[8] D. Ouyang, B. He, A. Ghorbani, N. Yuan, J. Ebinger, C. P. Langlotz, P. A. Heidenreich, R. A. Harrington, D. H. Liang, E. A. Ashley *et al.*, "Video-based ai for beat-to-beat assessment of cardiac function," *Nature*, vol. 580, no. 7802, pp. 252–256, 2020.

[9] W. Dai, X. Li, X. Ding, and K.-T. Cheng, "Cyclical self-supervision for semi-supervised ejection fraction prediction from echocardiogram videos," *IEEE Transactions on Medical Imaging*, vol. 42, no. 5, pp. 1446–1461, 2022.

[10] M. M. Kazemi Esfeh, C. Luong, D. Behnami, T. Tsang, and P. Abolmaesumi, "A deep bayesian video analysis framework: towards a more robust estimation of ejection fraction," in *International Conference on Medical Image Computing and Computer-Assisted Intervention*. Springer, 2020, pp. 582–590.

[11] R. Muhtaseb and M. Yaqub, "Echocotr: Estimation of the left ventricular ejection fraction from spatiotemporal echocardiography," in *International Conference on Medical Image Computing and Computer-Assisted Intervention*. Springer, 2022, pp. 370–379.

[12] S. Thomas, A. Gilbert, and G. Ben-Yosef, "Light-weight spatio-temporal graphs for segmentation and ejection fraction prediction in cardiac ultrasound," in *International Conference on Medical Image Computing and Computer-Assisted Intervention*. Springer, 2022, pp. 380–390.

[13] M. Mokhtari, N. Ahmadi, T. S. Tsang, P. Abolmaesumi, and R. Liao, "Gemtrans: A general, echocardiography-based, multi-level transformer framework for cardiovascular diagnosis," in *International Workshop on Machine Learning in Medical Imaging*. Springer, 2023, pp. 1–10.

[14] R. e. a. Varudo, "Machine learning for the real-time assessment of left ventricular ejection fraction in critically ill patients," *Critical Care*, 2022.

[15] C. D. Fraleigh and E. Duff, "Point-of-care ultrasound: An emerging clinical tool to enhance physical assessment," *The Nurse Practitioner*, 2022.

[16] M. Heidari, R. Azad, S. G. Kolahi, R. Arimond, L. Niggemeier, A. Sulaiman, A. Bozorgpour, E. K. Aghdam, A. Kazerouni, I. Hacihaliloglu *et al.*, "Enhancing efficiency in vision transformer networks: Design techniques and insights," *arXiv preprint arXiv:2403.19882*, 2024.

[17] M. Fiaz, M. Heidari, R. M. Anwer, and H. Cholakkal, "Sa2-net: Scale-aware attention network for microscopic image segmentation," *arXiv preprint arXiv:2309.16661*, 2023.

[18] J. Yang, Y. Lin, B. Pu, J. Guo, X. Xu, and X. Li, "Cardiacnet: Learning to reconstruct abnormalities for cardiac disease assessment from echocardiogram videos," in *European Conference on Computer Vision*. Springer, 2025, pp. 293–311.

[19] Y. Sadegheih, A. Bozorgpour, P. Kumari, R. Azad, and D. Merhof, "Lhunet: A light hybrid u-net for cost-efficient, high-performance volumetric medical image segmentation," *arXiv preprint arXiv:2404.05102*, 2024.

[20] T. Liu, Q. Yang, Y. Zhang, R. Ge, Y. Chen, and G. Zhou, "Think as cardiac sonographers: Marrying sam with left ventricular indicators measurements according to clinical guidelines," in *International Conference on Medical Image Computing and Computer-Assisted Intervention*. Springer, 2025, pp. 575–584.

[21] The Cardiovascular. Ejection fraction (ef): Physiology, measurement & clinical evaluation. [Online]. Available: <https://ecgwaves.com/topic/ejection-fraction-ef-physiology-measurement-echocardiography/>

[22] H. Reynaud, A. Vlontzos, B. Hou, A. Beqiri, P. Leeson, and B. Kainz, "Ultrasound video transformers for cardiac ejection fraction estimation," in *Medical Image Computing and Computer Assisted Intervention-MICCAI 2021: 24th International Conference, Strasbourg, France, September 27–October 1, 2021, Proceedings, Part VI 24*. Springer, 2021, pp. 495–505.

[23] R. R. Selvaraju, M. Cogswell, A. Das, R. Vedantam, D. Parikh, and D. Batra, "Grad-cam: Visual explanations from deep networks via gradient-based localization," in *Proceedings of the IEEE international conference on computer vision*, 2017, pp. 618–626.

[24] A. P. Kalogeropoulos, G. C. Fonarow, V. Georgiopoulou, G. Burkman, S. Siwamogsatham, A. Patel, S. Li, L. Papadimitriou, and J. Butler, "Characteristics and outcomes of adult outpatients with heart failure and improved or recovered ejection fraction," *JAMA cardiology*, vol. 1, no. 5, pp. 510–518, 2016.

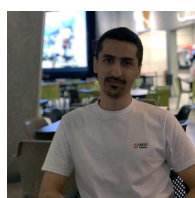
[25] M. Carroll, "Ejection fraction: Normal range, low range, and treatment," Nov 2021. [Online]. Available: <https://www.healthline.com/health/ejection-fraction>



**Moein Heidari** received the Bachelor of Science (B.Sc.) and Master of Science (M.Sc.) degrees in Electrical Engineering from the Iran University of Science and Technology (IUST), Tehran, Iran, in 2021 and 2023 respectively. He is currently a Ph.D. student with the School of Biomedical Engineering, University of British Columbia (UBC), Vancouver, BC, Canada. His research lies broadly at the intersection of machine learning and medical imaging, with emphasis on generative and large language models.



**Afshin Bozorgpour** received the MSc degree in information technology with a specialization in network science from the University of Tehran, Iran, in 2021. Currently, he is pursuing his doctoral research with the Faculty of Informatics and Data Science, University of Regensburg, Germany. His primary research interests lie in the intersection of deep learning, generative models, medical image processing, and computer vision.



**Amirhossein Zarif** received the B.Sc. degree in Electrical Engineering from the Iran University of Science and Technology (IUST), Tehran, Iran. His research interests lie in artificial intelligence with a focus on image processing and its applications in the medical domain. Following his undergraduate studies, he transitioned into the field of AI, where he has been actively engaged in developing expertise in computer vision, deep learning, and machine learning techniques for healthcare and biomedical applications.



**Wenjin Chen** had a Bachelor of Medicine degree from Beijing Medical University (now Peking University Medical Center) and a Ph.D. degree from the Program of Molecular Biosciences at Rutgers University. Her research experience included tissue microarray image analysis, pathology image processing, pattern recognition, robotic telemicroscopy, as well as medical information systems and clinical data warehouses. Dr. Chen oversees the imaging services and leads the clinical data warehouse team at Biomedical Informatics Division at Rutgers Cancer Institute. She has extensive experience in designing and implementing medical informatics workflows and databases and leads several research projects in the areas including digital pathology, remote education, pathology informatics and oncology clinical data warehouse.



**Ilker Hacihaliloglu** (Member, IEEE) received the B.Sc. and M.Sc. degrees from Istanbul Technical University, Istanbul, Türkiye, in 2001 and 2004, respectively, and the Ph.D. degree from The University of British Columbia, Vancouver, BC, Canada, in 2010. Following his doctorate, he worked as a Postdoctoral Fellow with the Center for Hip Health and Mobility and Vancouver General Hospital, Vancouver, from 2010 to 2013. From 2014 to 2021, he was a Faculty Member with the Department of Biomedical Engineering and served as an Adjunct Faculty Member with the Department of Radiology, Rutgers University, New Brunswick, NJ, USA. He is currently an Associate Professor with the Department of Radiology and Department of Medicine, The University of British Columbia. His core research mission is to advance innovation in artificial intelligence (AI) for applications in both industrial and clinical services and products.



**Dorit Merhof** is a full professor and head of the Institute of Image Analysis and Computer Vision, Faculty of Informatics and Data Science, University of Regensburg, Germany. Her research interests include deep learning, biomedical image processing, and computer vision.



**David J. Foran** is currently a Professor of pathology Laboratory Medicine and Radiology and the Chief of the Division of Medical Informatics, Rutgers Robert Wood Johnson Medical School, New Brunswick, NJ, USA. He also serves as Executive Director of Computational Imaging and Biomedical informatics and Chief Informatics Officer at the Rutgers Cancer Institute, New Brunswick. His research interests include the design, development, and implementation of new approaches in computer-assisted

diagnostics, medical imaging, and statistical pattern recognition for resolving challenging clinical problems in pathology, radiology, and oncology.



**Dr. Jasmine Grewal** is a clinical associate professor at the University of British Columbia and a member of the Divisions of Cardiology at St. Paul's Hospital and Vancouver General Hospital. Dr. Grewal has fellowship training in adult congenital heart disease/pregnancy and heart disease (Toronto General Hospital) and echocardiography (Mayo Clinic, Rochester). Dr. Grewal focuses her clinical time in the care of adults with congenital heart disease, pregnant women with cardiac disease, echocardiography and in the St. Paul's Hospital Cardiac Intensive Care Unit. Dr. Grewal is actively engaged in clinical research, and is currently involved as a primary and co-investigator in numerous single centre and multi-centre research studies in the areas of congenital heart disease and pregnancy and heart disease.

**Dr. Jasmine Grewal** is a clinical associate professor at the University of British Columbia and a member of the Divisions of Cardiology at St. Paul's Hospital and Vancouver General Hospital. Dr. Grewal has fellowship training in adult congenital heart disease/pregnancy and heart disease (Toronto General Hospital) and echocardiography (Mayo Clinic, Rochester). Dr. Grewal focuses her clinical time in the care of adults with congenital heart disease, pregnant women with cardiac disease, echocardiography